6 Field Measurement

6.1 Introduction

This chapter consist of two parts, firstly a description of the methodology of this measurement and its setup. The second part of this chapter will present the comparison and analysis of the calculated and measured results. Measured ankle currents will also be shown in this chapter. Measured EMF distribution was compared with the field measurements in order to validate the findings in Chapter 4. The correlation between field measurements in the near zone of the Skelton C curtain array antenna 766 and modelling results is important as a means of validating the work presented in this thesis.

6.2 Measurement methodology setup

In order to investigate the relationship between the field strength and the actual levels of SAR within the human body it was necessary to measure the vertically and horizontally polarized E-field separately. Several practical problems, in connection with the field measurement, were addressed during an initial field trip to the Skelton C (Penrith, Cumbria, UK) transmission site. The site is located in an open uncontrolled rural area surrounded by dozens of adjacent MF, HF and VLF antennas. For this reason there will inevitably be some interference from other antennas. These measurements were made in close proximity to a 300kW HF broadcasting array. For this reason, unlike in other EMF measurements scenarios, the power levels encountered in the region of interest are very high. Moreover, in order to minimise unwanted interference, humans need to be at least 6-7 meters away from the measurement point. The outdoor measurement set-up needed to be configured so as to minimize EM interference within an uncontrolled environment. The set-up also needed good all-weather capability. Given the considerations listed above, it became apparent that none of the commercially available EM measurement probes would be suitable for this application. A new measurement system was thus custom designed for this research study. The system is comprised of a receive antenna, a non-perturbing transmission line and a spectrum analyser. In was important to ensure that the new

measurement system was a cost efficient and reliable to ensure reproducibility. It was also desirable to develop a system that could be applied in other high power HF transmission site field measurements. Fig 6.1 shows the schematic diagram for the measurement system, developed in this chapter.

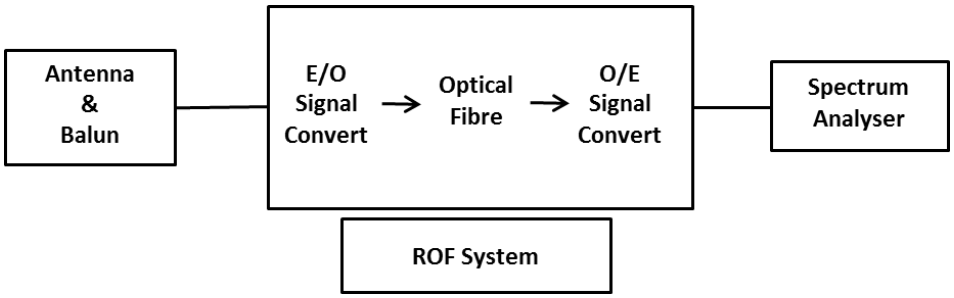

Fig 6.1 Schematic diagram of Radio over Fibre (RoF) measurement system.

At the receiving end a simple telescopic whip antenna was connected to an off-shelf balun (Diamond HF Bun-50). The length of the whole receive antenna could be extended up to a maximum of 4m. This design allows the antenna to be adjusted according to the measured signal where is necessary and increases the ease of transportation. These field measurements used the fully extended length. The receive antenna was mounted bolted to a rotatable hinge on top of a tripod. This allowed the antenna to be rotated through 90 ° for the purpose of making measurements in the vertical or horizontal plane. The whole supporting structure was made from plastic in order to avoid any unnecessary blockage and/or reflections. The commercially available E-field probes were unsuitable, as mentioned earlier. The reason for this is that they would either be unable to tolerate this extremely high power level or were designed for using at higher frequencies. The antenna chosen for this application would be able to pick-up the desired signal, the setup of which is shown in Fig 6.2.

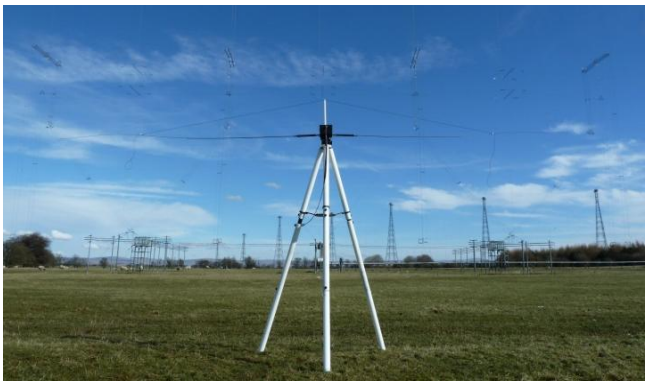

Fig 6.2 Receive antenna.

A radio-over-fiber (RoF) link was employed to relay the signal from the receive antenna to the spectrum analyzer. RoF has attracted much attention as a convenient way of distributing and transmitting microwave signals. It is widely used in wireless and cellular communications systems [6.1], [6.2]. When a coaxial cable is used in a high field strength environment it can have detrimental effects on the measurement. These could include reflections from the surface of the cable as well as blockage. The coupling of electromagnetic fields into the cable would also lead to undesired induced currents. Depending on the signal wavelength, the magnitude of the induced current is proportional to the length of the coaxial cable. It would be possible to reduce the current by using a shorter cable, but this would mean that the human operator would need to be situated much closer to the receive antenna. This is undesirable because the human operator must be situated at least 6-7 meters away from the receive antenna in order to avoid distortion of the field by the human body. The RoF alleviates this problem by enabling the spectrum analyzer to be located at a good distance from the receive antenna. The fiber optic cable is almost invisible to the radio frequency signal. In this measurement system a transmitter box was connected to the receive antenna. The transmitter and receiver circuits were housed within shielded metal boxes. The dimensions of these boxes were 11.5cm x 9cm x 5cm. Within the measured frequency range, any effects that might be caused by the metal box can be ignored. A photodiode (Plastic Fiber Optic Transmitter Diode SFH756) within the transmitter box is used to convert the electrical signal from the receive antenna into an optical signal. It also filters unwanted noise and passes the signals to the band of interest. This signal is then transmitted over a 15 meter long optical fiber cable into the receiver box (Fig 6.3a). At the other end of the system a receiver box containing an O/E (Optical signal to Electrical signal) reverse circuit was attached to a hand-held spectrum analyzer (Rohde & Schwarz FSH3 Spectrum Analyser). The reverse circuit consists of a photo-detector (Plastic Fiber Optic Photodiode Detector SFH 250) and a high transimpedance amplifier (OPA380) chip, as shown in Fig 6.3b.

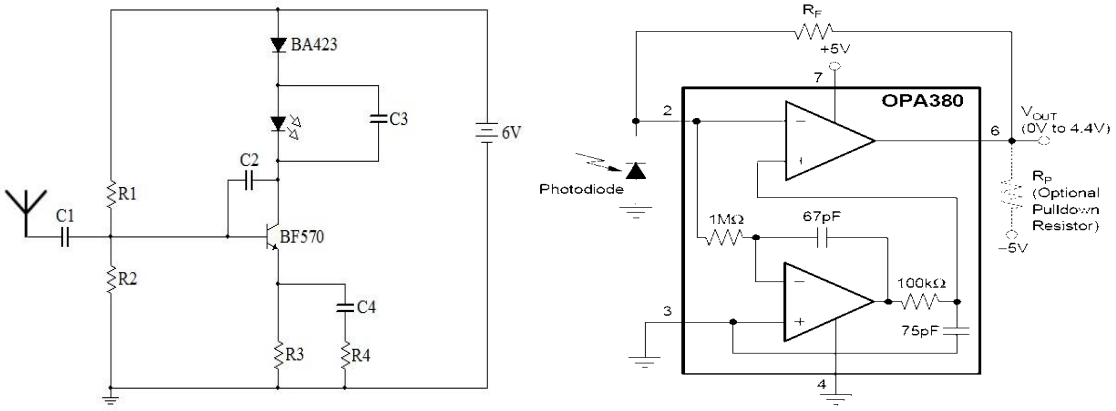

a) The transmitter box b) The receiver box [6.3]

Fig 6.3 Transmitter and receiver schematic diagram of the RoF system.

The measurements reported in this chapter were conducted in the near-field of the antennas. In this region the power level is very high. For that reason, and in order not to distort the measurement, a new piece of measurement equipment was developed, as discussed above. This chapter also justifies the methodology and equipment used for measurement. The whole system setup is shown in Fig 6.4.

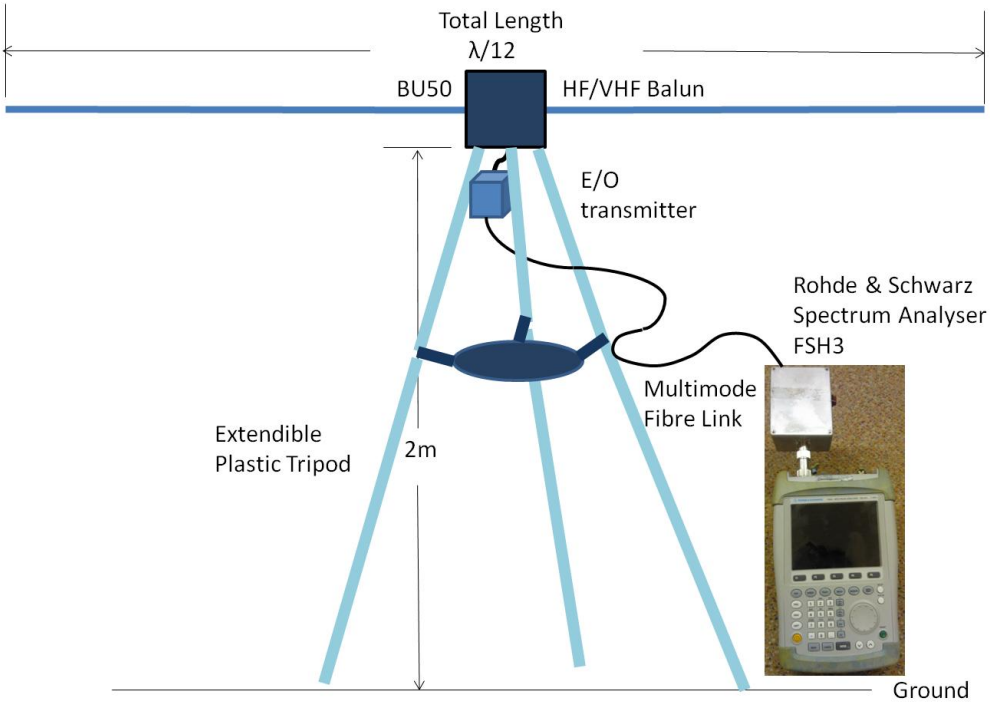

Fig 6.4 Whole measurement system.

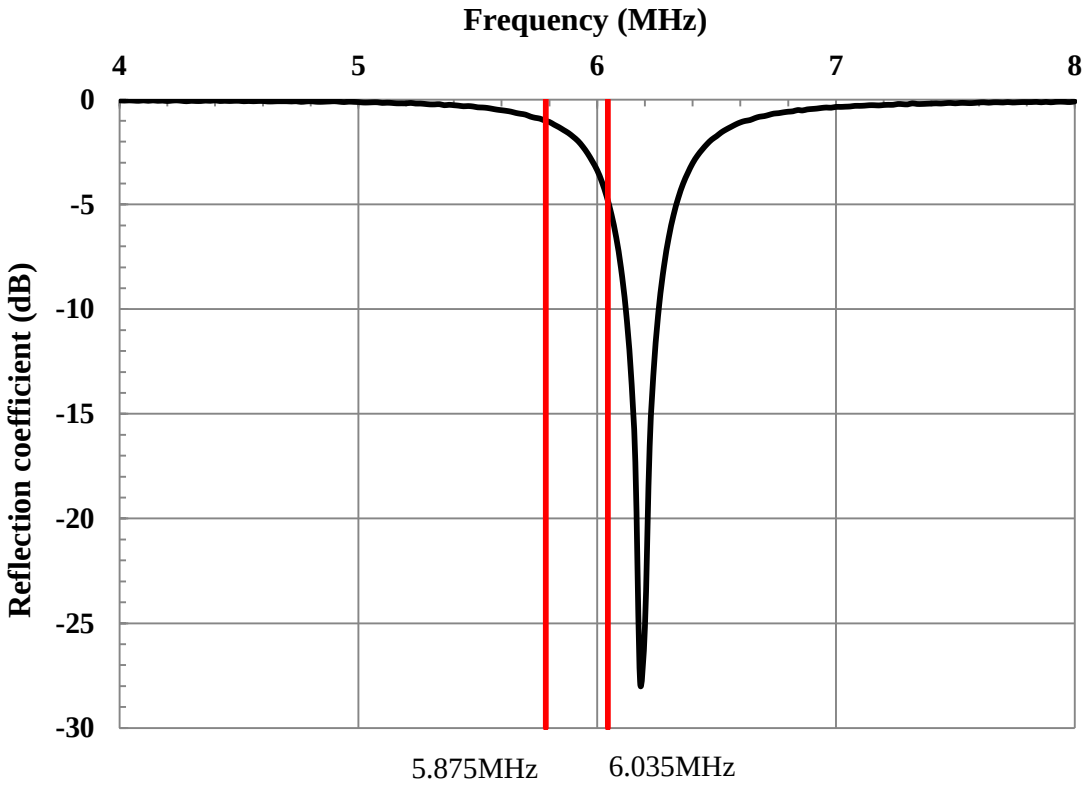

Fig 6.5 Reflection coefficient of receive antenna (dB).

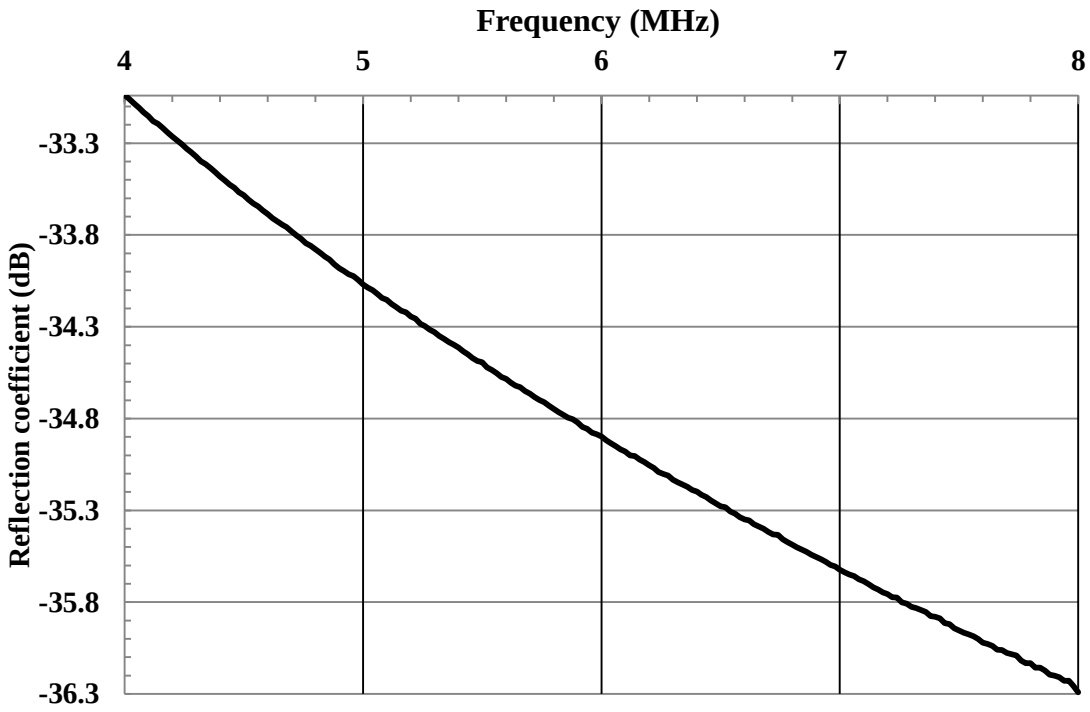

Fig 6.6 Forwarding scattering parameters of RoF system (dB).

The measured plain carrier wave frequencies were 5.875MHz and 6.035MHz. The reflection coefficient of the receive antenna between frequency 4-8MHz is shown in

Fig 6.5. There is a strong resonance at around 6.2MHz. The return loss remains below 8dB over the frequency range between 6.1MHz to 6.3MHz. The insertion loss was about 35dB around the measured frequencies. The signal source measured here is a high power transmitter (300kW). The E-field component level in some of the 'hot spots' could be 60 V/m as predicted or even higher, with the power level around 49dBm. However, the maximum power of the Rohde & Schwarz FSH3 portable Spectrum Analyser is only 20dBm (or 30 dBm (1 W) for max. 3 minutes) [6.4]. The RoF system was able to prevent the damage to the spectrum analyser. A calibrated antenna is not required because we are not attempting to measure the exact values of the power. Instead the intension is to compare the shape and pattern of power distribution obtained through measurement with that derived from simulation. Precaution had to be taken to avoid overloading the spectrum analyser. For this reason it is unnecessary to restrict operation to the narrowband of frequencies over which the antenna is well matched. The transmitting antennas at different sites operate on different frequencies in a range (5-22MHz). However it would still be possible to use this simple dipole antenna at those sites as it can be operated over a fairly wide band of frequencies.

The measurement locations chosen were those that were expected to feature high and significantly varying field strengths. These locations were predicted using the models developed in Chapter 4, specifically the model chosen was the whole antenna and array infrastructure with 0.4 ground slope and a ground condition (AVG) (ε_r = 13 and σ = 0.005 S/m) (Fig 6.7). Fig 6.8 is the vertically and horizontally polarized E-field distributions for this model at a height of 2 metres, with red lines indicating the selected measurement regions.

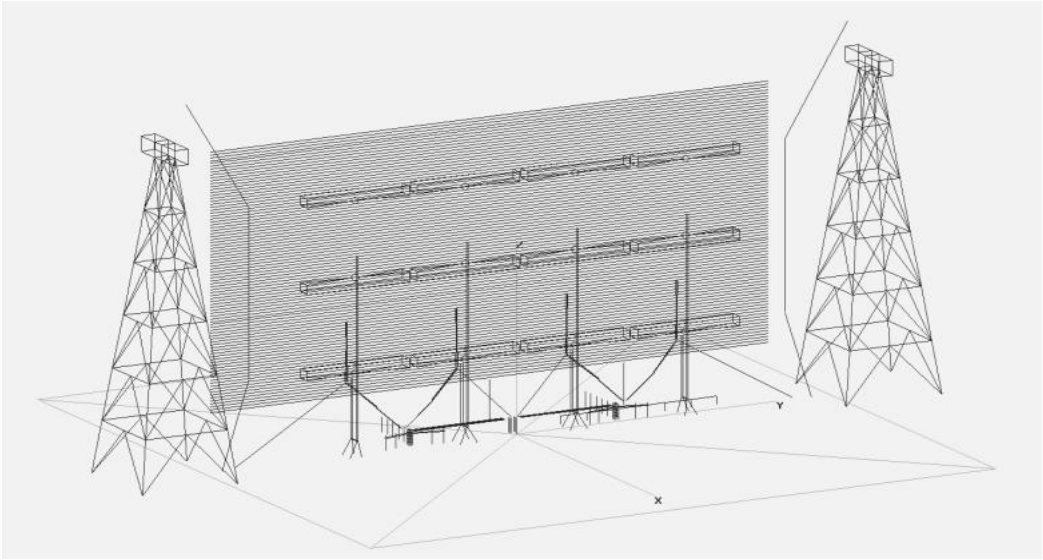

Fig 6.7 NEC model of Skelton C HF curtain array antenna 766 with 0.4 ground slope and array infrastructure.

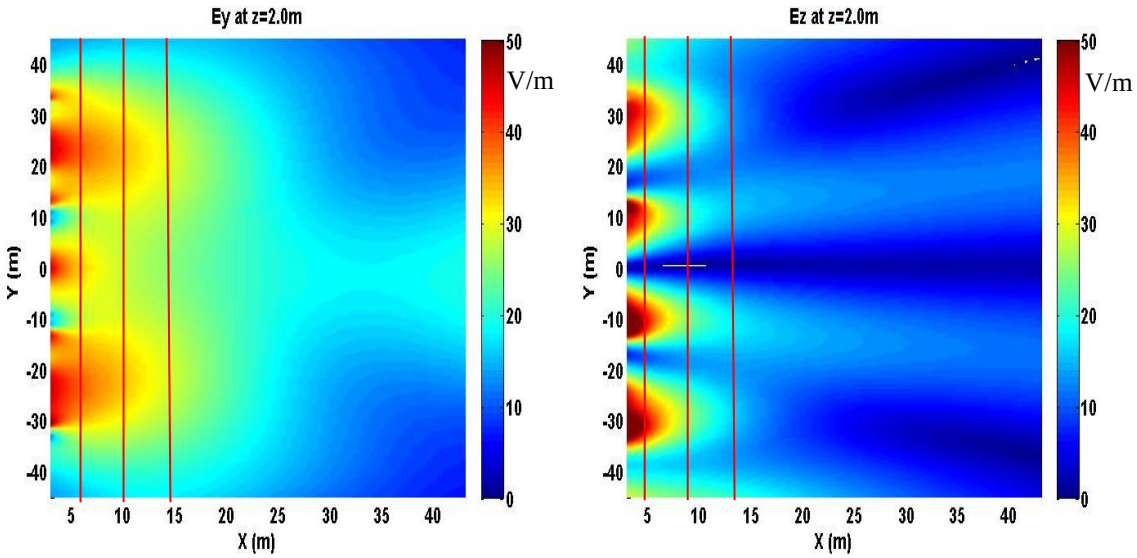

a) Ey at 2 m above ground b) Ez at 2 m above ground

Fig 6.8 Predicted horizontal and vertical E-field distributions and three preselected lines in front of array for measurements at x=6m, 10m, 15m.

The measurements were made by scanning a plane 2m above the ground across three linear rows, parallel with and at three different distances (6m, 10m and 15m) from the Skelton C HF curtain array antenna 766, as shown in Fig 6.9**Error! Reference source not found.**. Mapping of the locations can be seen in Fig 6.10. The E-field values were measured at 5 meter intervals along the rows while the ankle current was determined at 2.5 meter intervals. Ey and Ez were measured separately at each point on the line. The

female and male were both were both wearing ordinary wellington boots. The body size and height of the humans used in the measurement were similar to those of the voxel human phantom employed in Chapter 3, for ankle current (HI-4416 Numeric EMF Readout Unit [6.5]) measurements the assessment of whole-body SAR.

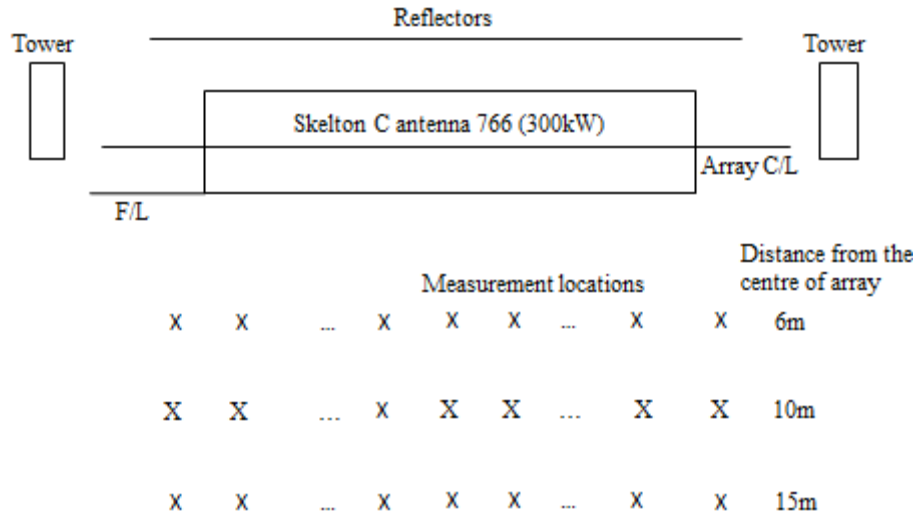

Fig 6.9 Overview of the mapped locations in front of the array.

Fig 6.10 Mapping measurement locations in front of antenna.

6.3 Comparisons of calculated results and measured results

The measured E-field distributions are shown in Fig 6.11 (Ez) and Fig 6.12 (Ey). Ideally this graph would be symmetrical about the 0 degree axis. In practice the pattern is asymmetrical due to the slope in the ground terrain in front of the antenna. The vertically polarised E-field rises to a peak at ±45m and attains its minimum value in the centre (i.e. approximately 0 degrees). The measurement and simulation results are

compared in Fig 6.16 and Fig 6.17. From Fig 6.13 to Fig 6.15 compare male and female ankle currents at different distances in front of array. The shape of the ankle current curves for the male and female subject is similar. However generally the value of ankle current is lower in the female, due to the smaller body size, this is consistent with the simulated results shown in chapter 3. The biological composition of male and female ankles is essentially identical but the overall cross sectional size is different. This leads to a difference in the current density. The measurement therefore proves that the induced current in the ankle region is related to its size. There is good agreement between the general shapes of the graphs shown in Fig 6.11, and 6.13 to 6.15. In all four graphs the highest level are at ±45m within the measured range, a trough at around 0 degrees and a local maximum at approximately -15 degrees. This indicates that the graph obtained using the system designed for this study have good agreement with those produced using our custom designed measurement set-up. This serves in part to validate the new system developed for the purpose of this research.

Because the measurement system was not calibrated, results of both graphs should not be seen as the actual E-field strength value. Fig 6.11 and Fig 6.12 should only consider the shape and pattern of the measured results. To compare simulation and measurement results, Fig 6.17 and Fig 6.18 values used peak normalization to compare the pattern and shape differences.

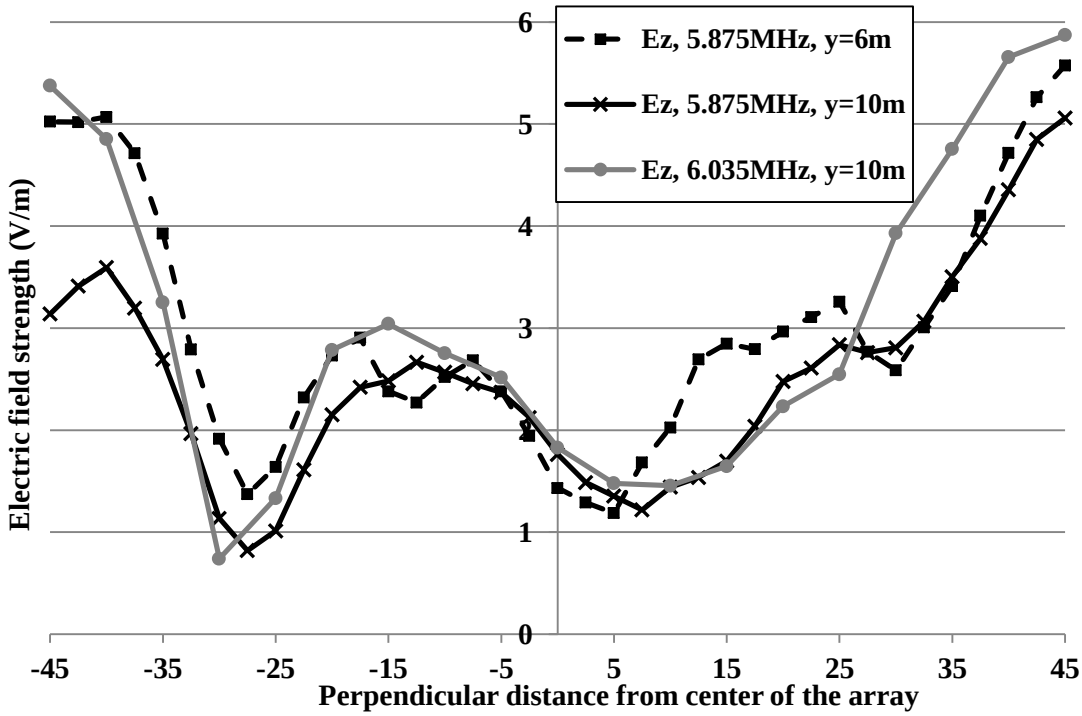

Fig 6.11 Measured vertically polarized E-field.

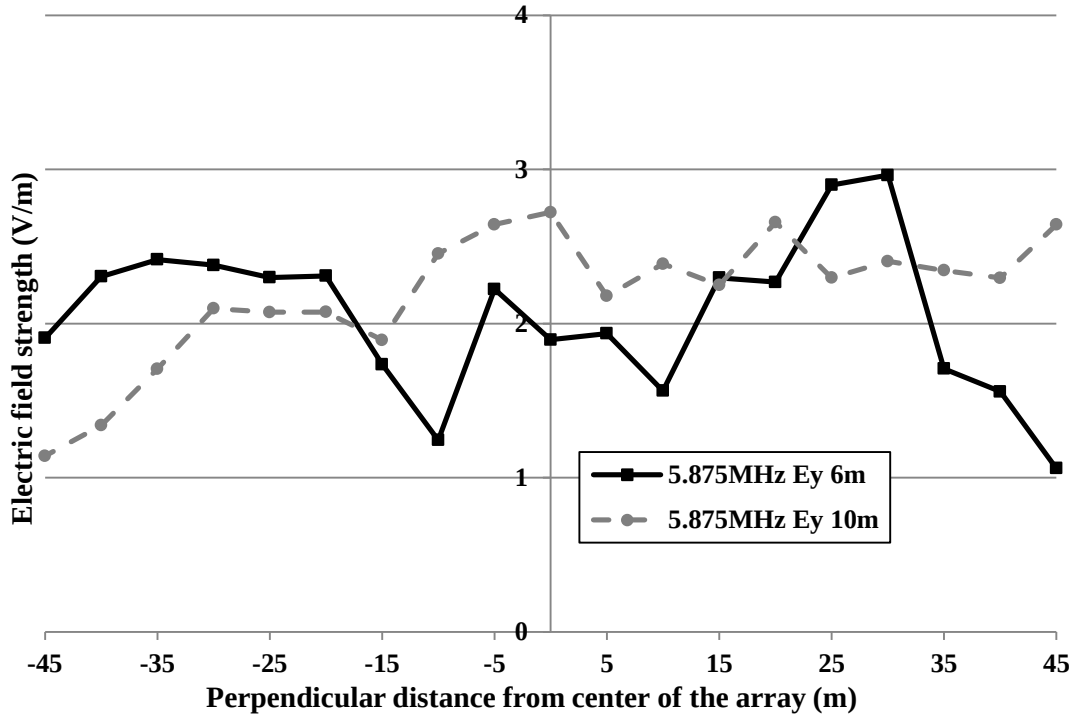

Fig 6.12 Measured horizontal polarized E-field.

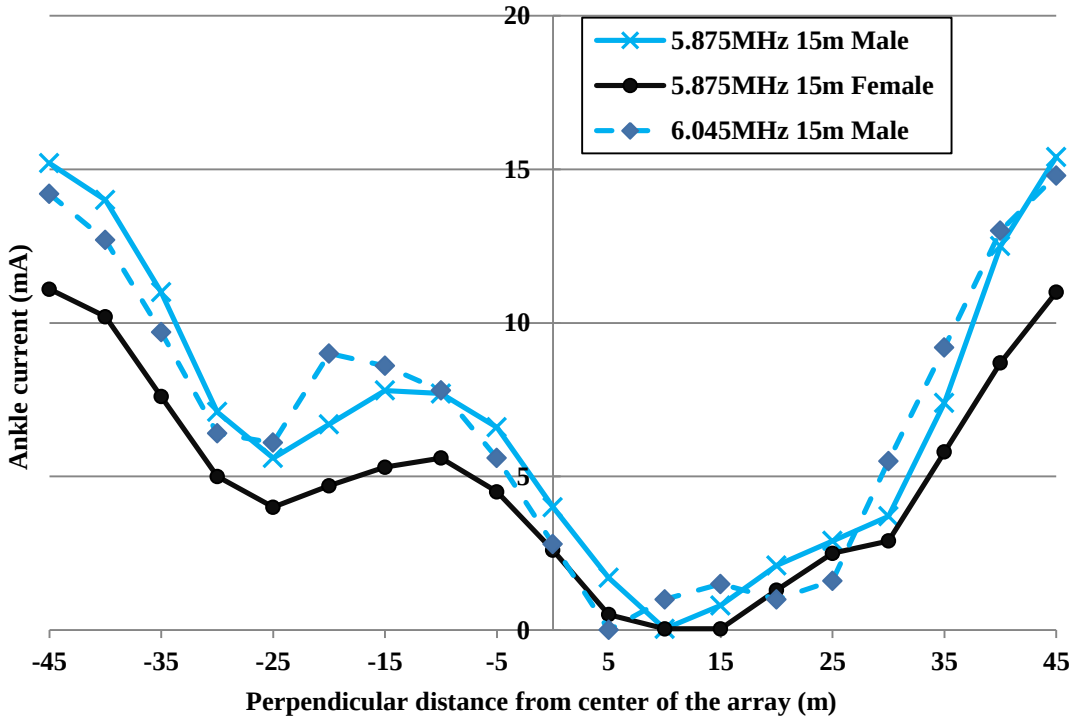

Fig 6.13Measured ankle current 15m in front of array.

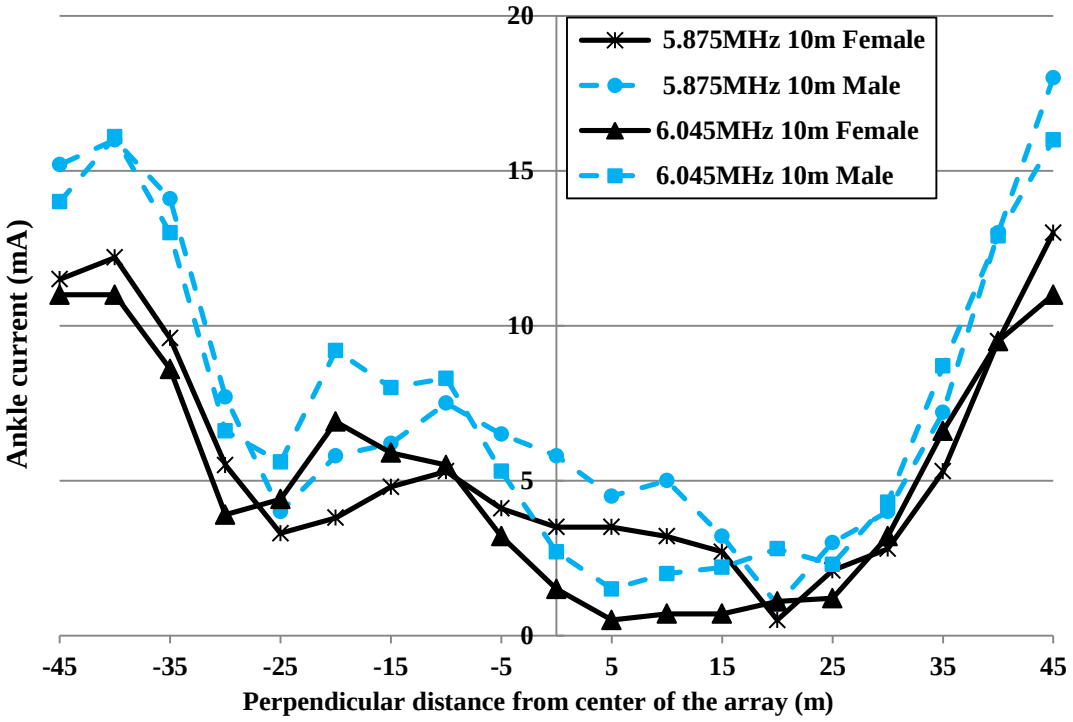

Fig 6.14Measured ankle current 10m in front of array.

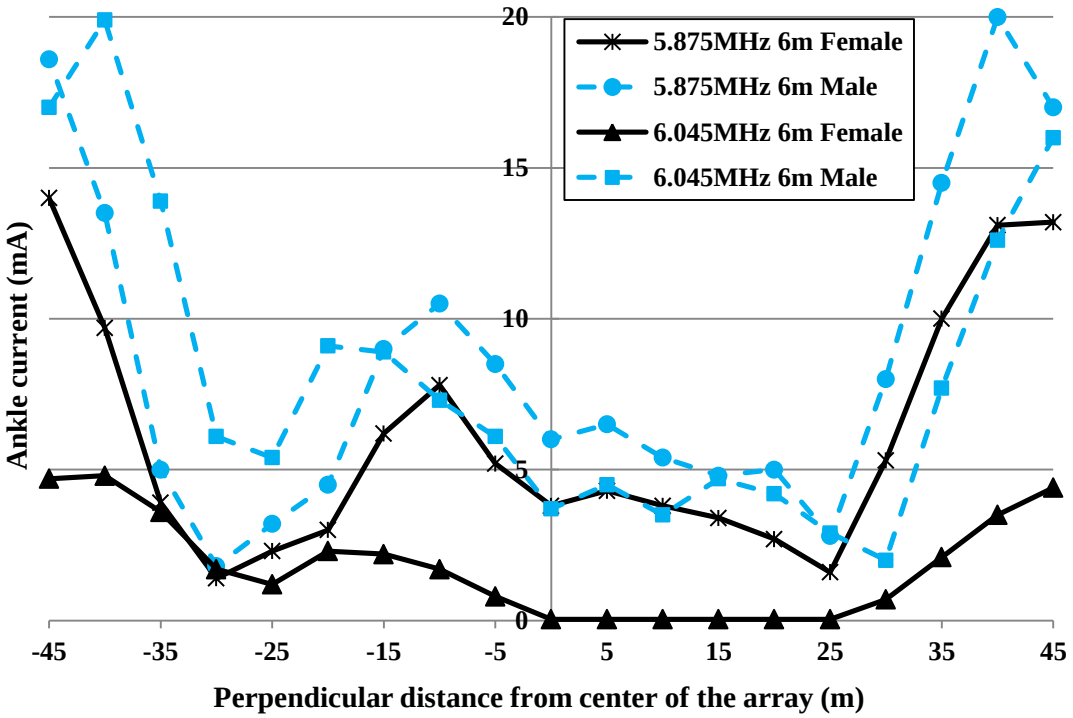

Fig 6.15 Measured ankle current 6m in front of array.

The measured ankle currents and Ez values had similar changing trends. Measured ankle currents of the female were consistently lower than the males results when compared at the same distance in front of array. This demonstrated the results

presented in chapter 3. Around the ankle region, the ankle current is directly related to the strength of the vertical field component and ankle size.

Furthermore the comparison of the nomalised field distributions, obtained through simulation and measurement, is shown in Fig 6.16 (Ez) and Fig 6.17 (Ey). The NEC4 models compared in these figures relate to model for a self-supporting tower and above an average (AVG) ground. Two ground slope angle models were used in the comparisons (i.e. 0.4 °and 2 °).

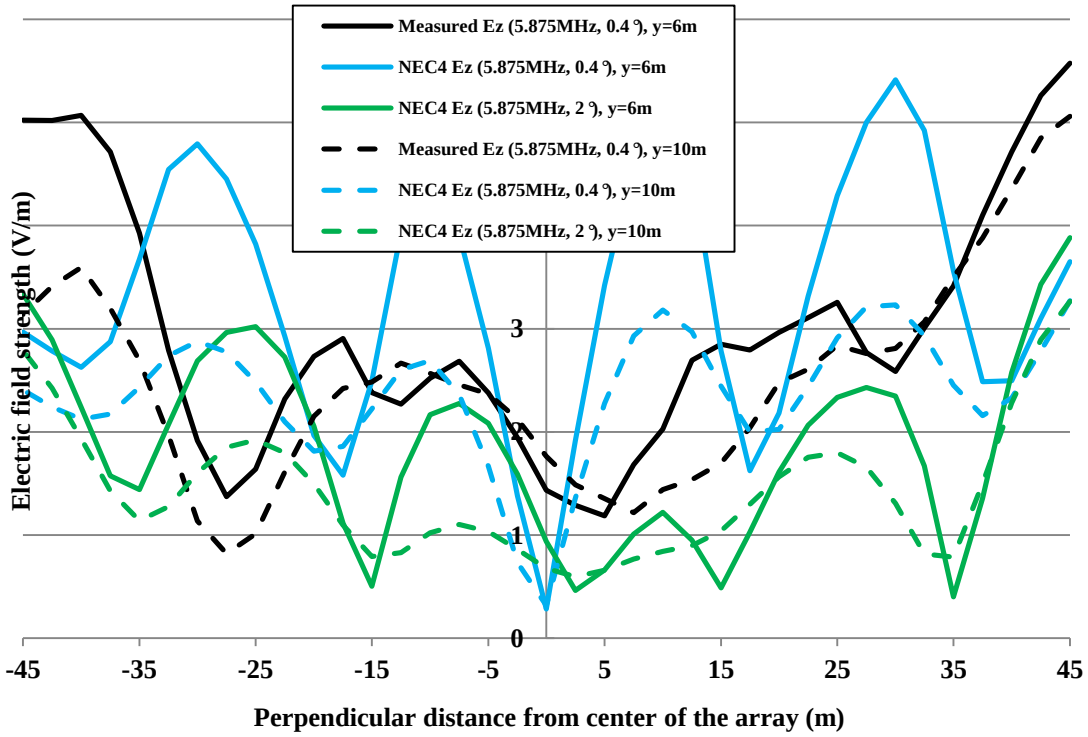

Fig 6.16 Comparisons of the vertical measured E-field with NEC4 simulated model with 0.4 ° & 2 ° ground slope model.

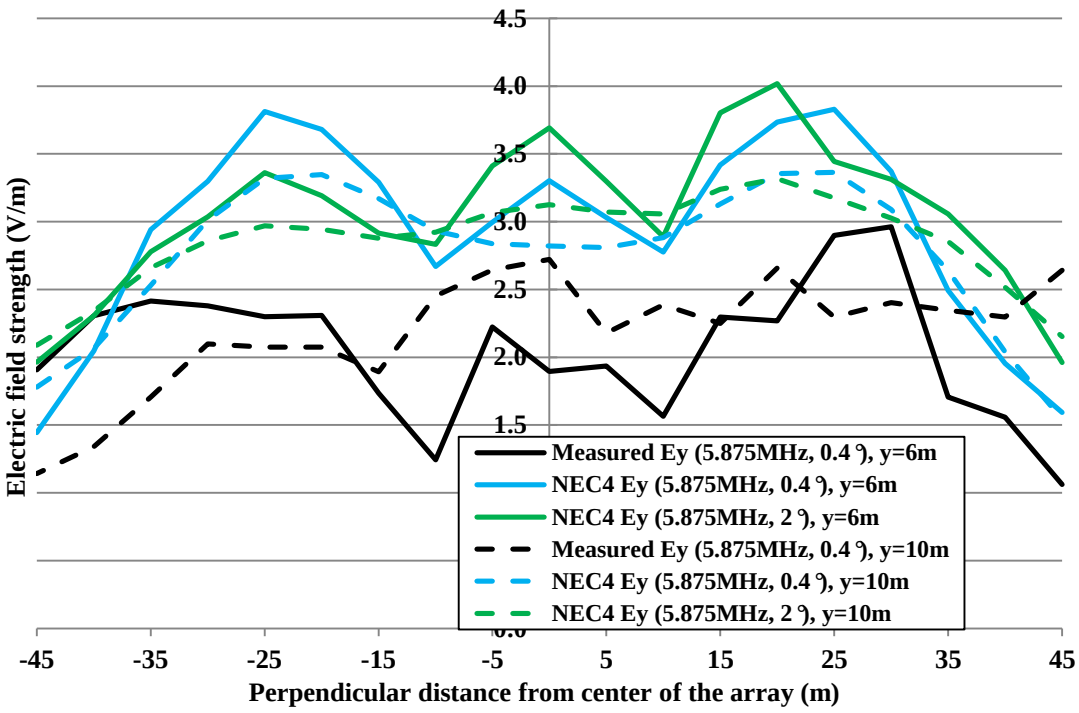

Fig 6.17 Comparisons of the measured horizontal E-field with NEC4 simulated model with 0.4 °& 2 °ground slope model.

The ground slope at the test site is 0.4 degrees. For that reason the curves obtained through measurement were expected to agree best with those derived through simulation using a ground slope of 0.4 degrees. However in practice the measurements agree best with the curves obtained through simulation using a ground slope of 2 degrees. This unexpected finding could be attributed to differences between the exact profile of the real ground terrain and that simulated. In Figs. 6.16 and 6.17 there are a greater number of asymmetric variations within ±30 degrees of the centre of the antenna. This is the region in which most of the infrastructure is located, further investigation on effects of these would provide more information about their effect on the field. At ± 30 m perpendicular to the centre of antenna, measured results show relatively lower values than those at each end of the antenna. In chapter 4, it was discovered the presence of the vertical metal scatters underneath the antenna reduce the size of the area where the field values were high. Referring to Pocklington's Integral Equation [6.6], the total field would be sum of incident and scattered fields. The structure's effects on the vertical and horizontal electric field components depends on their locations and length, especially when the measurement points are very close to them. In the site, there are more structures that were not included in the modelling; only some main structures were considered to study their effects on the e-field. The

results here have shown good agreements with the findings in previous chapters. Studies in chapter 4 showed that the ground can have a significant effect on the results. For this reason the factors listed above could account for the differences observed.

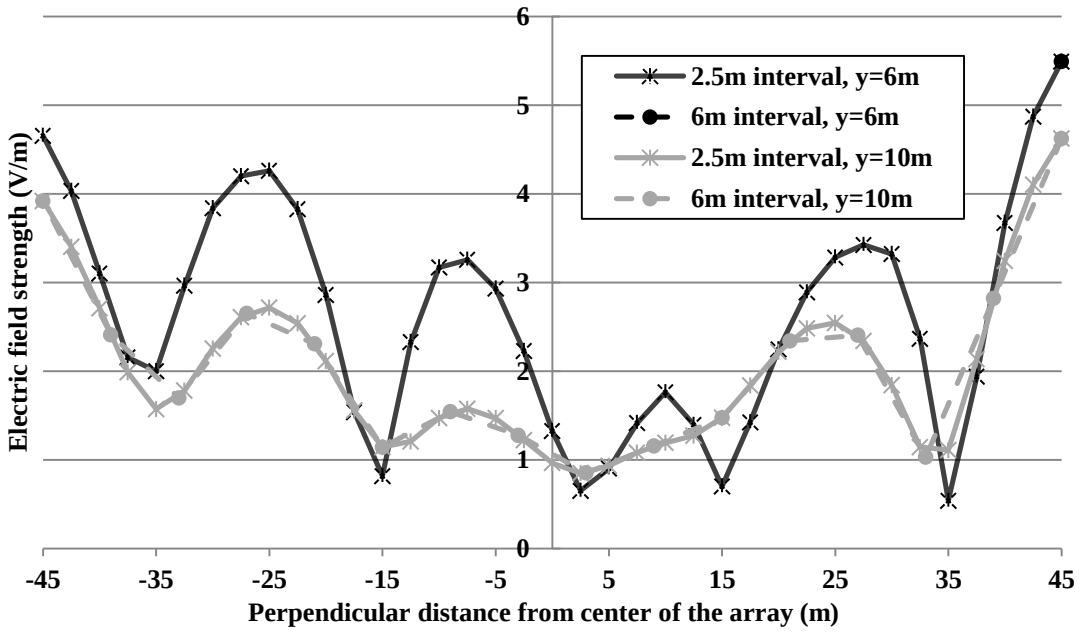

Fig 6.18 Comparisons of NEC4 simulated fields sampling at varies rate.

All of the simulation results presented in Fig 6.18 were obtained at 0.5 meter intervals along the lines shown in Fig 6.8 (i.e. using a 0.5 m computational grid). Subsequently certain points were selected from the result, at intervals of 6m, 7m, or 2.5m. The resulting curves are shown in Fig 6.18. On closer inspection of Fig 6.18 there does not appear to be an overall trend in these results. However it is clear that the choice of sampling points can have a significant effect on the amplitude values and pattern shape. This has implications for the selection of the measurement grid used in simulation and measurement. Reducing the space between points in the measurement grid might be beneficial because it is clear that some information is lost when using a coarser grid.

In a previous chapter, the WBSAR and ankle current values were calculated with the plane-wave radiating the heterogeneous numerical phantoms. Human phantoms were considered with various ground conditions. By re-applying the method and increasing the incident plane-wave to 40&60 V/m, which is the same as the simulated 300kW measured array, the comparisons of calculated ankle current and whole-body SAR were shown in Fig 6.19. Here a highly moist ground condition was also used with

dielectric properties of $\varepsilon_r = 30$ and $\sigma = 0.005$ S/m. Based on the results, Fig 6.20 present the derived electric field levels required to produce the measured ankle current.

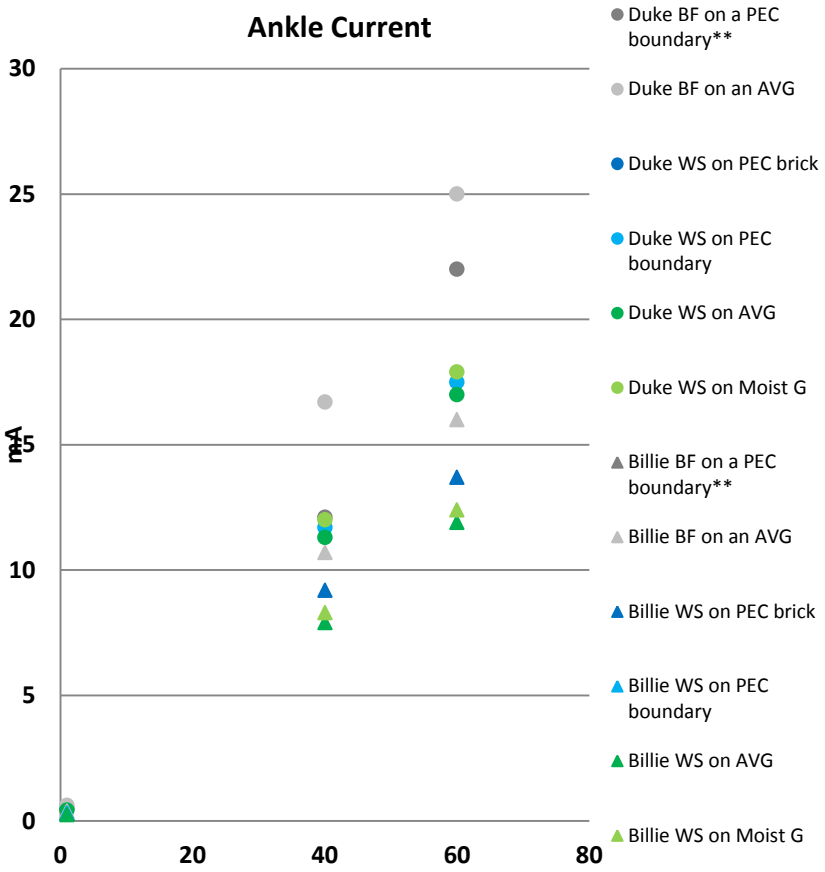

a) Calculated ankle current (mA) of heterogeneous human models in various ground conditions.

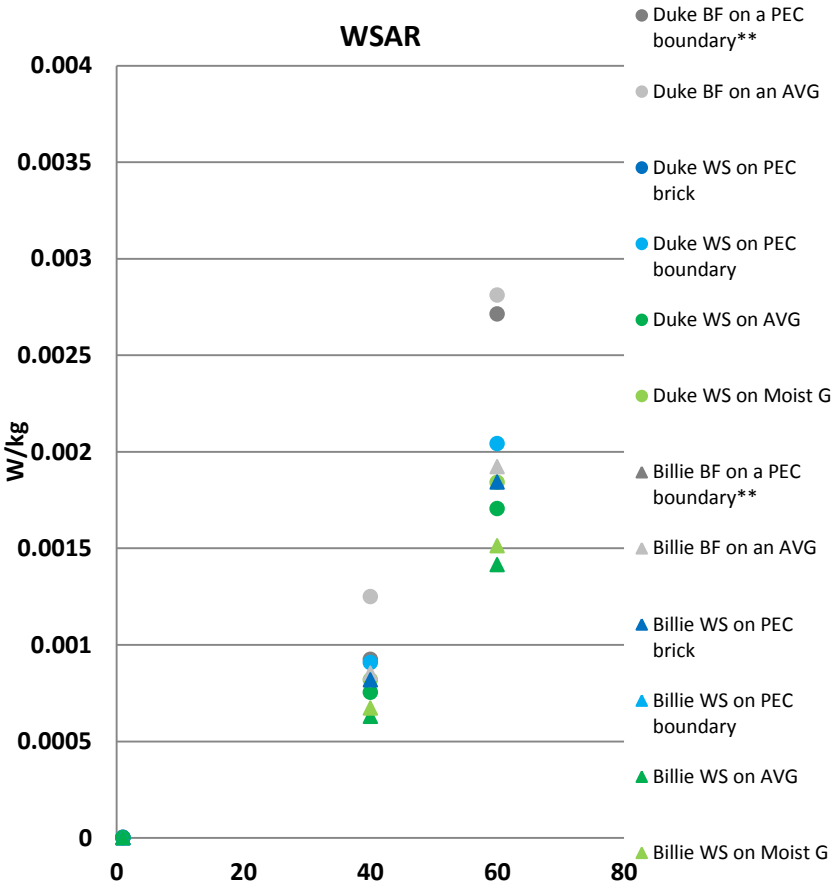

b) Calculated whole-body averaged SAR (W/kg) of heterogeneous human models in various ground conditions.

Fig 6.19 Plane-wave irradiation on human phantoms at 1V/m, 40V/m and 60V/m.

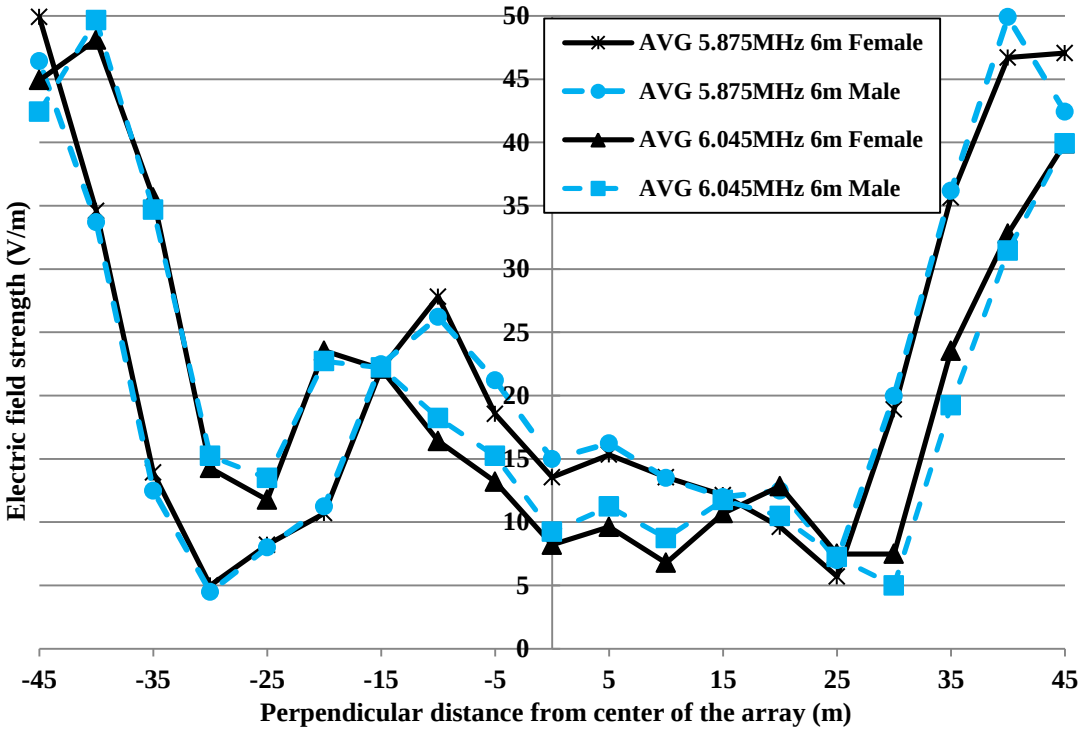

a) Derived Ez (V/m) levels required to produce measured ankle current level when human standing 6m in front of array on average ground.

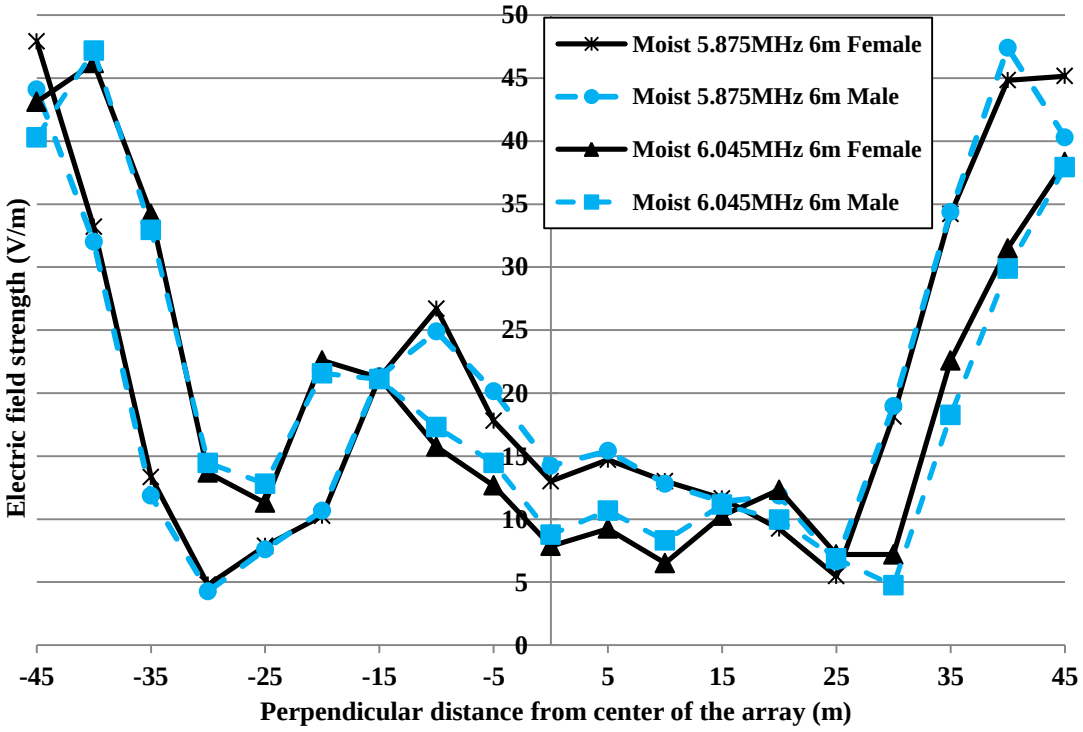

b) Derived Ez (V/m) levels required to produce measured ankle current level when human standing 6m in front of array on moist ground.

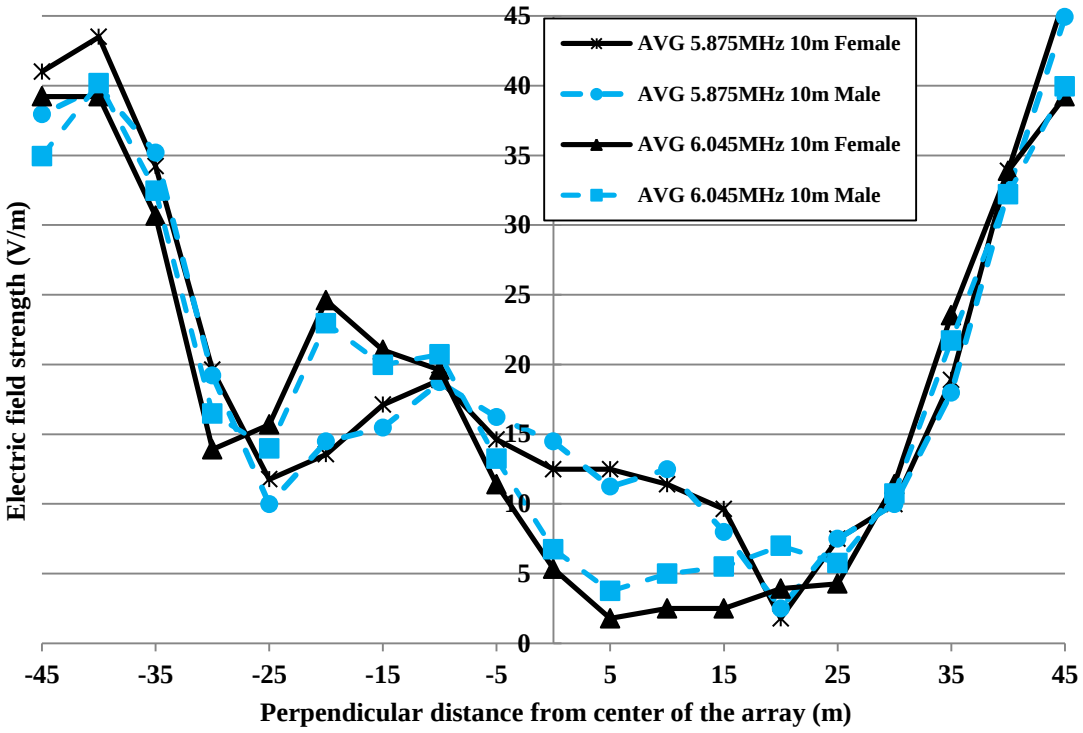

c) Derived Ez (V/m) levels required to produce measured ankle current level when human standing 10m in front of array on average ground.

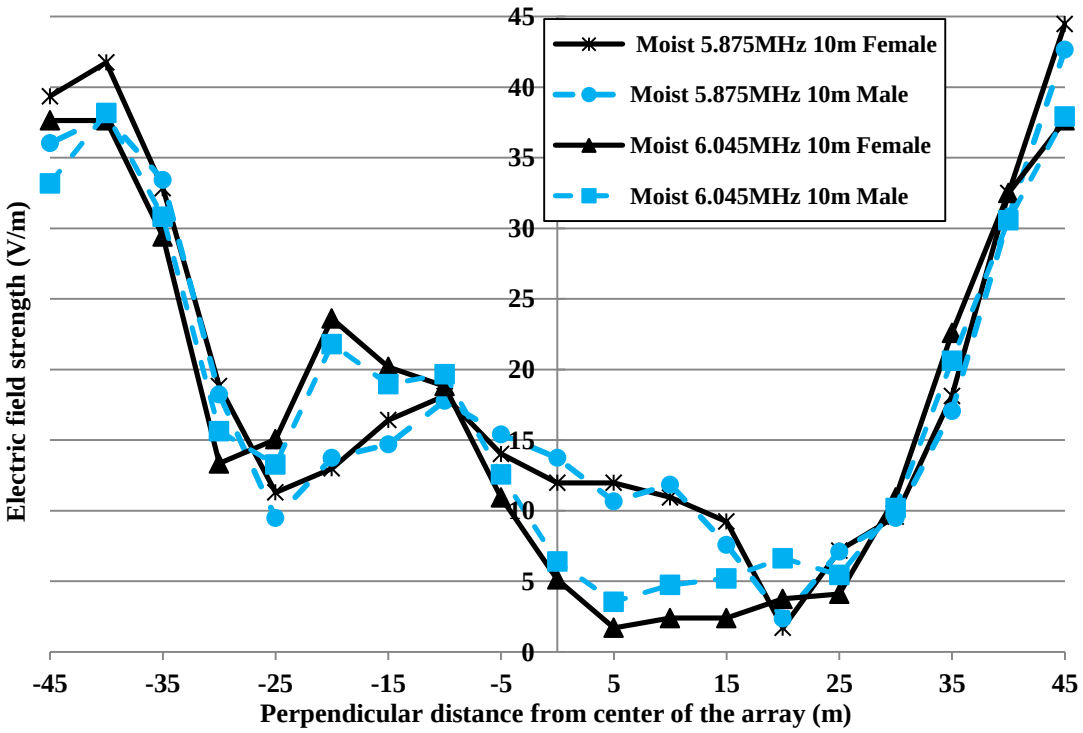

d) Derived Ez (V/m) levels required to produce measured ankle current level when human standing 10m in front of array on moist ground.

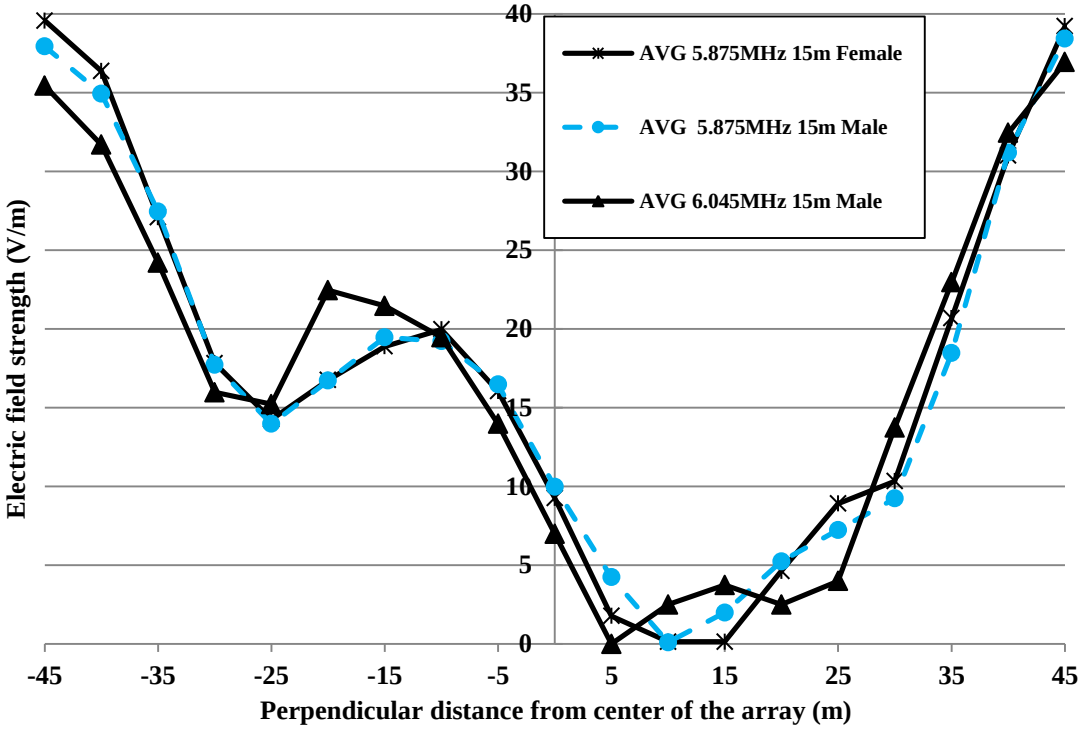

e) Derived Ez (V/m) levels required to produce measured ankle current level when human standing 15m in front of array on average ground

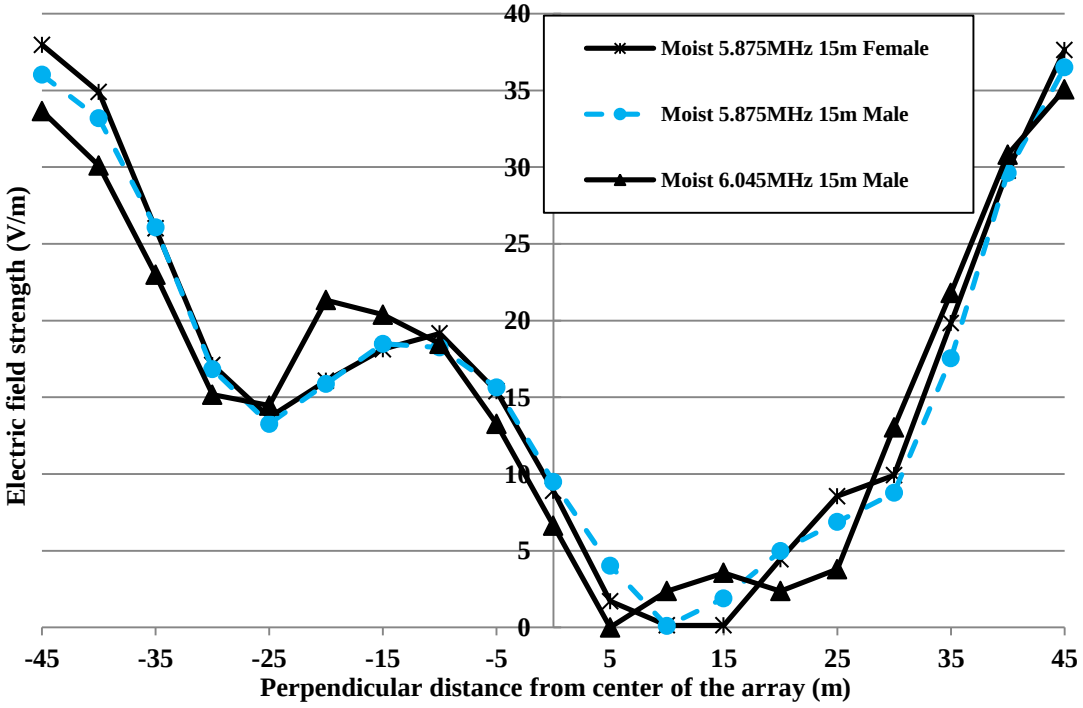

f) Derived Ez (V/m) levels required to produce measured ankle current level when human standing 15m in front of array on moist ground

Fig 6.20 Derived electric field levels Ez(V/m) required to produce measured ankle current level with human standing in front of array for AVG and Moist ground.

where AVG: average condition ground (ε_r = 13 and σ = 0.005 S/m)
Moist G: Moist Ground (ε_r = 30 and σ = 0.005 S/m)

In Fig 6.19 the highest ankle current and WBSAR appear when both female and male humans are barefoot perfectly grounded; these are +3dB higher than human standing on a lossy ground. Male has higher ankle current and WBSAR level than female. Even the worst case of barefoot grounded, the WBSAR of both female and male are maximum 0.003 W/kg. This is much smaller compared with the International Commission on Non-Ionizing Radiation Protection (ICNIRP) occupational basic restriction (0.4 W/kg) and reference level (0.08 W/kg). Considering the humans wearing shoes on a ground plane would be a realistic scenario, the WBSAR of male is only 2 mW/kg and less than 1 mW/kg for female. Despite the ground condition differences, the SAR level of human exposure is proportional to the frequency dependent incident E-field level. Linear interpolation was employed to derive the required electrical field levels to produce the measured ankle current levels in Fig 6.20 a-f. The derived electric field levels which were required to produce measured ankle current level provided a direct comparable correlation between the measured results and calculated results. These also established WBSAR and E-field level calculation in the case of human exposure at HF broadcasting transmitters in compliance with ICNIRP guidelines.

6.4 Conclusions

This chapter describes the methodology and equipment used during the field measurements. The purpose of the field measurements presented in this chapter was to validate the findings in chapter 4. Analysis of the results reveals that the spatial distribution of E-field, recorded using the ankle current probe, agrees well with that obtained using the custom designed measurement set-up. This helps to validate the new measurement set-up. The results obtained through measurement and simulations were also compared in this chapter. According to the construction drawings the ground slope at the test site is 0.4 degrees. For this reason it was anticipated that the measurement results would agree best with those obtained through simulations employing a ground slope of 0.4 degrees. However it was discovered that the measurement results agree best with the simulation results pertaining to a ground slope of 2 degrees. This could be attributed to factors that were not accounted for in the simulations, or due to dimensional errors on the test antenna which deviate from those specified in the drawings. Other factors include: the exact profile of the ground terrain,

infrastructure associated with the transmitter, and heavy precipitation in the air on the day of the test which also had the effect of making the ground very wet and so changing its electrical conductivity. These would all contribute to the difference between the measured and simulated results. However, from the above observation the measurement system has good performance and achieved the aim of design which was to validate the E-field distributions predicted by simulation. The measured results provide useful information on validating the finding of this thesis.

References

[6.1] S.-C. Chan, S.-K. Hwang, and J.-M. Liu, "Radio-over-fiber AM-to-FM upconversion using an optically injected semiconductor laser," *Opt. Lett.*, vol. 31, no. 15, p. 2254, 2006.

[6.2] Y. Josse, B. Fracasso, and P. Pajusco, "Model for energy efficiency in radio over fiber distributed indoor antenna Wi-Fi network," pp. 131–135.

[6.3] "Precision High-Speed Transimpedance Amplifier OPA 380." [Online]. Available: http://www.ti.com/lit/ds/symlink/opa380.pdf.

[6.4] R. & Schwarz, "R&S FSH3, R&S FSH6, R&S FSH18 Data Sheet."

[6.5] "Holaday Numeric EMF Readout Unit." [Online]. Available: https://www.ets-lindgren.com/HI-4416.

[6.6] C. A. Balanis, *Antenna Theory: Analysis and Design*, Third Edit. John Wiley & Sons, Inc., 2005, p. 34.